

# **High-speed Coherent Fourier Scatterometry** Galvo mirror integration for fast surface inspection

Soman, Sarika; Horsten, Roland C.; Pereira, Silvania F.

10.1016/j.measurement.2025.119294

**Publication date** 

**Document Version** Final published version

Published in

Measurement: Journal of the International Measurement Confederation

Citation (APA)
Soman, S., Horsten, R. C., & Pereira, S. F. (2026). High-speed Coherent Fourier Scatterometry: Galvo mirror integration for fast surface inspection. Measurement: Journal of the International Measurement Confederation, 258, Article 119294. https://doi.org/10.1016/j.measurement.2025.119294

# Important note

To cite this publication, please use the final published version (if applicable). Please check the document version above.

Other than for strictly personal use, it is not permitted to download, forward or distribute the text or part of it, without the consent of the author(s) and/or copyright holder(s), unless the work is under an open content license such as Creative Commons.

Takedown policy

Please contact us and provide details if you believe this document breaches copyrights. We will remove access to the work immediately and investigate your claim.

ELSEVIER

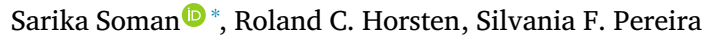
#### Contents lists available at ScienceDirect

# Measurement

journal homepage: www.elsevier.com/locate/measurement



# High-speed Coherent Fourier Scatterometry: Galvo mirror integration for fast surface inspection



Delft University of Technology, Faculty of Applied Sciences, Department of Imaging Physics, Lorentzweg 1, Delft, 2628CJ, The Netherlands



Keywords: Scatterometry High-speed Optical metrology

#### ABSTRACT

Coherent Fourier Scatterometry (CFS) is a powerful optical metrology technique for the precise characterisation of nanostructures. Conventional CFS systems rely on piezo-based scanning stages for raster scanning, which limits throughput due to slow scanning speeds. In this work, we present a high-speed CFS system incorporating a galvanometric (galvo) mirror for beam scanning. This approach significantly enhances scanning speed while maintaining measurement accuracy. Although galvo mirrors are widely used in optical systems, their implementation in CFS has unique challenges such as off-axis beam aberrations and angle-dependent beam shifts at the split detector. These issues are analysed and mitigated through optical design, alignment and system calibration. Additionally, we derive the minimum detector bandwidth required to capture high-frequency signals generated by the fast scanning. The effectiveness of the system is demonstrated through the calibration of pits with various diameters that are etched onto a silicon wafer. Results show a substantial improvement in scanning speed as compared with piezo-based systems without compromising measurement precision, making this approach highly suitable for high-throughput metrology applications.

#### 1. Introduction

Nanostructures have become foundational in various fields such as electronics, health care, automotive industry, and material science [1–9]. For example, nanostructures are integral to the semiconductor industry, where billions of nanoscale transistors on a single chip enable the power and efficiency needed in modern computing and communications [1,2]. As these applications evolve, high-speed metrology tools are essential for good process control and yield optimisation. They can also support the timely implementation of corrective actions that reduce downtime during production by providing faster insights into process variations [1].

Traditional metrology methods such as scanning electron microscopy (SEM) or atomic force microscopy (AFM) often struggle to keep pace with high-throughput production environments due to long acquisition times, stringent measurement conditions, and destructive or contact-based measurements [10]. These limitations can create bottlenecks during the production process. Optical metrology tools such as scatterometry, white-light interferometry, and confocal microscopy offer alternative solutions which can be used for fast, non-contact measurements in high-throughput environments [11,12].

For decades, optical scatterometry, a model-based optical metrology tool, has been a workhorse in the semiconductor industry used to obtain critical dimensions of structures in-line during fabrication [13].

Scatterometry involves collecting and analysing light scattered from a surface to infer its properties. Coherent Fourier scatterometry (CFS), the method used in this work, is an advanced form of optical scatterometry, in which the scattered field from a range of incident plane waves is recorded simultaneously [14]. It uses an objective lens to transform a coherent collimated light beam into a focused spot on the sample. Each point within the back focal plane (BFP) of the objective or the Fourier plane corresponds to a distinct angle of incidence. The scattered field, reflected from the sample, is captured by the same objective lens. The field at the Fourier plane is then recorded using a camera for further analysis. The recorded far-field (field at the Fourier plane) acts as a signature from which the geometric properties of the sample can be retrieved.

The CFS technique has also been extended to isolated sub-wavelength particle detection where the CCD camera is replaced by a split-detector to detect asymmetries in the far-field [15]. For this application, the surface to be inspected is raster scanned and a point-by-point differential signal is obtained from the split-detector. Despite its advantages, CFS systems for particle detection face challenges in high-throughput applications due to their reliance on piezo-based scanning stages for moving the focused spot across the sample surface. While this approach provides high sensitivity to sub-wavelength nanostructure

E-mail address: s.soman@tudelft.nl (S. Soman).

<sup>\*</sup> Corresponding author.

 Table 1

 Side-by-side comparison of different surface-inspection tools.

Technique	Scan time for $100\mu m \times 100\mu m$	Pros	Cons
AFM	Very slow. Scan time ≈27.7 min for pixel size of 10 nm and 60 kHz feedback loop bandwidth [21].	Excellent lateral and vertical resolution; Absolute 3D topography; Compatible with different surfaces.	Slow with limited field of view; Needs regular tip replacement due to tip wear; Can be potentially damaging to sample surface;
SEM	Slow. Scan time $\approx 75\mathrm{s}$ with dwell time of $10\mu\mathrm{s}$ and pixel size $36.6\mathrm{nm}$ [22].	Excellent lateral resolution; Elemental and crystallographic studies possible.	Stringent measurement conditions; requires high/ultra-high measurement conditions; charging effects for non-conducting samples; can cause sample contamination due to carbon deposition.
Dark-field	Very fast. Scan time $\approx 0.003  s$ for a system using 193 nm wavelength to detect contaminants >35 nm <sup>a</sup> [23].	High throughput; High sensitivity to scatterers; Simple optics design.	Require high laser power; Dynamic range limits detection near edges due to detector saturation; Model-based inference; Difficulty in measuring low-contrast particles.
Confocal microscopy	Fast. Scan time of $\approx 0.06 \mathrm{s}$ with a pixel size of $100 \mathrm{nm}$ using rotating polygons [24].	Good lateral and axial resolution.	Complicated optical system; Low signal-to-noise ratio for small and low contrast particles; Correction required for off-axis beam aberrations.
CFS — piezo-based	Slow. Scan time $300  s$ for a system with pixel size of $100  nm^b$ .	Good lateral resolution and axial resolution; High sensitivity to low-contrast scatterers; Simple optics design; Low power ideal for delicate samples; Possible to retrieve the size and shape of sub-wavelength nanostructures [25,26].	Slow; Model-based inference.
CFS — galvo-based (Proposed)	Fast. Scan time 1s for a system with 100 nm pixels.	Same as piezo-based system.	Correction required for off-axis beam aberrations; Tighter alignment requirements; Model-based inference.

<sup>&</sup>lt;sup>a</sup> Polystyrene latex (PSL) particle equivalent.

measurement capabilities, it is time-consuming, particularly for large surface areas or applications requiring rapid analysis. Addressing this limitation is thus essential to facilitate the broader adoption of CFS in commercial settings.

Previously, we proposed using parallel probes to reduce scan time for a certain area proportionally to the number of probes [16]. However, in this configuration, each probe requires separate detection and acquisition channels, increasing the electronic complexity as the number of beams increases.

In this study, we investigate the use of a galvo mirror for fast beam scanning. Galvo mirrors are known for their precise and high-speed beam positioning capabilities. They are widely used in applications, such as laser cutting, LIDAR, and microscopy, to enable rapid, controlled beam movement [17–20]. In our new system, we replace the piezo stage used in the fast axis of the raster scan with a galvo mirror for beam scanning, significantly reducing the total scan time. Table 1 shows a comparison of the proposed design with different surface-inspection tools in terms of throughput and general pros and cons.

Implementation of a galvo mirror scanning in a CFS setup presents unique challenges. In general galvo mirror implementations as a preobjective scanner, the mirror is placed in the BFP or in a plane conjugate to the BFP of the objective. If the mirror is shifted from this position, the beam at the detector starts having an angle-dependent shift [27,28]. For detection schemes using cameras or integrating detectors, this does not pose a big problem. However the CFS setup uses a differential detection scheme, in which the beam is incident in the middle of a photodiode bi-cell functioning as a split-detector. Any beam movement generates asymmetry which gets amplified resulting in a spurious non-zero differential signal. This places stricter alignment requirements on the positioning of the galvo mirror in the BFP. In this work, we derive the beam offset at the detector as a function of the galvo angle and shift in position from the BFP, detail its impact on the CFS signal and implement an alignment protocol to ensure proper placement of the galvo mirror within the optical system to minimise the offset at the detector.

In general, one of the biggest disadvantages of using a galvo mirror as a beam scanner is the off-axis beam aberrations [29]. This is a fundamental limitation of the technique and can only be minimised using well-corrected objectives or other compensation techniques [30,31]. This has been addressed in this work by experimentally defining and determining the range of acceptable angles of the galvo mirror based on the combined influence of different aberrations on the output signal.

High-speed scanning also requires a detector with sufficient bandwidth to record high-frequency signals. In this paper, we detail the calculations to derive the minimum bandwidth as a function of the galvo frequency and the optical properties of the CFS system. Finally, we demonstrate the application of the beam-scanning CFS system by calibrating the diameters of pits with various diameters etched into a Si wafer. The contribution to the measurement uncertainty from different components of the system is also discussed.

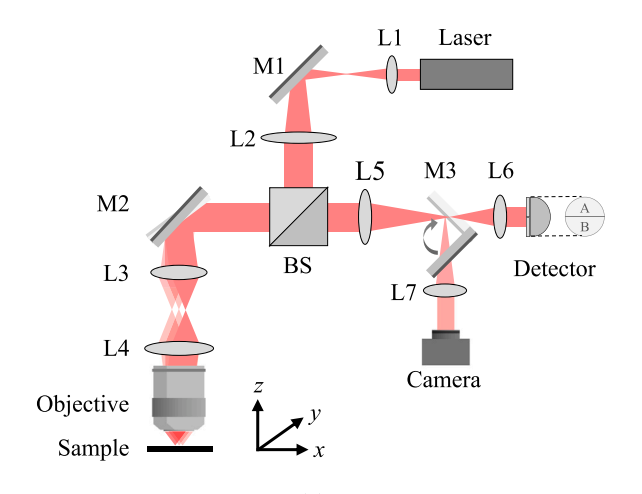
#### 2. Experimental setup

The schematic of the setup is shown in Fig. 1.

The laser beam from a 633 nm HeNe laser is expanded using lenses L1 (f = 10 mm) and L2 (f = 250 mm) in a telescopic arrangement. The expanded beam is scanned using a single-axis galvo mirror (GVS211/M, Thorlabs), M2, driven by a sinusoidal signal with maximum frequency of 1 kHz. The beam reflected from M2 is relayed to the BFP of the objective using lenses L3 (LSM03-VIS, Thorlabs) and L4 (TTL165-A, Thorlabs) also in a telescopic arrangement. The objective (N PLAN L 20x/0,40 NA, Leica) focuses the beam on the sample. The laser power at the focal plane was measured to be  $68\,\mu\text{W}.$ 

The light after reflection from the sample is captured by the same objective and de-magnified using lenses L5 (f = 275 mm) and L6 (f = 40 mm) in yet another telescopic arrangement. The lens pair relays the demagnified beam to the middle of the split-detector. Lenses L5 and L7 (f = 100 mm) are used similarly to de-magnify and relay the reflected beam to a CCD camera. A flipping mirror, M3, is used to switch between the detector and camera arm. The camera is used only to locate areas of interest on the sample.

<sup>&</sup>lt;sup>b</sup> Scan frequency = 1/35 of the first resonant frequency of the piezo (P-625.2 CD).



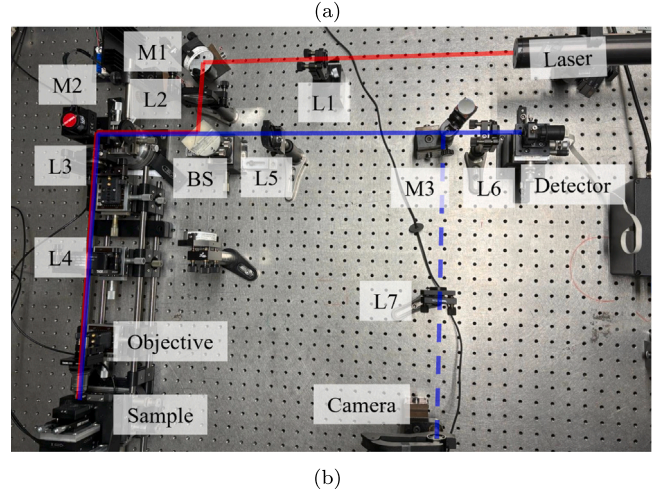


Fig. 1. (a) Schematic of the optical setup, (b) photo of the setup on the optical table: Red lines indicate the light path onto the sample and blue lines indicate the path of light after reflection from the sample to the detector. Dotted blue line indicates the reflected path to the camera. Lenses L1 - 10 mm, L2 - 250 mm, L3 - scan lens (LSM03-VIS, Thorlabs), L4 - tube lens (TTL165-A, Thorlabs), L5 - 275 mm, L6 - 40 mm, and L7 - 100 mm. Objective - 0.4 NA (N PLAN L 20x/0,40, Leica) objective lens, BS - beam splitter, M1 - mirror to fold light path, M2 - galvo mirror (GVS211/M, Thorlabs), M3 - flipping mirror to switch between camera and split-detection path, laser - 633 nm HeNe.

# 2.1. Split-detector

The split-detector consists of a bi-cell photodiode (SD 113-24-21-021). Each half of the bi-cell integrates the light incident on it. A differential signal is then generated by subtracting one diode signal from the other. When the incident beam is symmetric and falls in the middle of the bi-cell, the differential signal is zero. As the focused spot scans across an object, the scattered field becomes asymmetric and a non-zero differential signal is generated.

The point-to-point differential signal generated from the scan of an area containing a sub-wavelength feature, is shown in Fig. 2(a). The sample in the example consists of a Silicon wafer with a hole of 425 nm diameter and 60 nm depth etched into it. The spot size of the focused beam on the wafer (distance between first minima) is  $1.93 \, \mu m$ . The scan speed along the fast axis (*x*-axis) is  $15 \, \mu m/s$ , with a spacing of  $10 \, nm$  between successive scan lines (*y*-axis).

The detector signal from such a scan can be characterised by several parameters, including peak-to-peak voltage, signal width, and signal slope. For this study, only the peak-to-peak voltage is considered. The

peak-to-peak voltage of the signal is defined as the differential between the maximum and minimum values in the scan, measured in volts. Fig. 2(b) illustrates the cross-section through the peak of the scan, along with the definition of the peak-to-peak signal.

A symmetric differential signal has equal amplitudes for both the peak and valley relative to zero. A shift in the position of the beam relative to the midpoint of the bi-cell can introduce asymmetry in the differential signal. However, the peak-to-peak value of the signal remains unaffected [16].

# 2.2. 2D scanning and synchronisation

To obtain data such as shown in Fig. 2, the sample is raster-scanned in 2D using the galvo mirror in the fast axis (x) and a piezo stage (P-625.2 CD, Physik Instrumente) for the slow axis (y). The galvo mirror is driven using a sinusoidal wave of amplitude  $V_0$  and frequency f. The amplitude determines the width of the scan in the x-direction. The galvo angle is related to the applied voltage as 0.5 V/°. The extend in the y-direction is limited by the piezo range to 500 µm. The piezo stage is controlled such that the piezo in the slow-axis steps by  $\Delta y$  after one period of the galvo oscillation. An additional piezo stage (P-753.3, Physik Instrumente) is used for fine focus adjustments along the zaxis. There are also manual translational stages in three axes for coarse alignment. Both the galvo mirror and the y-piezo stage have different in-built sensors that can provide positional information for feedback. These feedback signals are used to assign x and y-coordinate information to the differential signal enabling us to create a 2D differential scattering map, as shown in Fig. 2(a) The differential signal along with the feedback signals are recorded using an ADC (NI 5734, National Instruments).

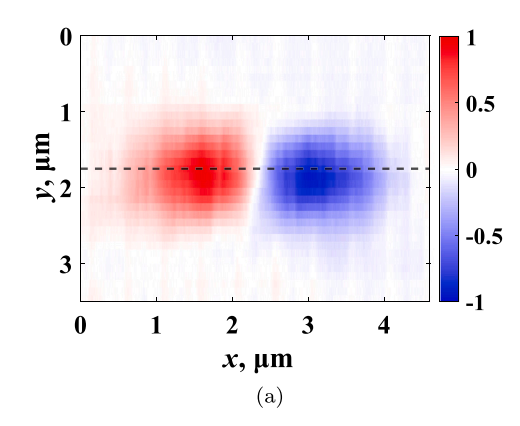
Fig. 3 shows an example of the different feedback signals of the galvo mirror and the *y*-piezo translator along with the differential signal as a function of time. The scan parameters for this example are:  $V_0$  - 800 mV, f - 100 Hz,  $\Delta y$  - 100 nm, sampling rate - 1 MHz. The measurement sample consists of a Si wafer with PSL (polystyrene latex) particles of 400 nm diameter.

# 3. Influence of the galvo mirror position

In the previous section we described the optical setup of the CFS system using the galvo mirror. There are two main details to consider while choosing the position of the galvo mirror within the setup: 1. After the deflection from the galvo mirror, the light after reflection from the sample must be de-scanned so that light beam remains parallel to the optical axis, 2. the position of the beam should not change relative to the split detector.

The first issue can be solved by having the galvo mirror positioned along the common optical path shared by both the incident and reflected beams. This configuration allows the galvo mirror to perform both scanning and de-scanning functions. When the galvo mirror rotates by an angle  $\theta$  about its axis, it deflects the incident beam by an angle  $2\theta$  relative to the optical axis (see Fig. A.12 in Appendix A). After interacting with the sample, the reflected beam travels back towards the galvo mirror at an angle of  $-2\theta$  with respect to the optical axis. The galvo mirror then introduces an additional  $2\theta$  deflection in the reflected path, realigning the beam to be parallel to the optical axis. Thus, by being located in the shared path of both incident and reflected beams, the galvo mirror effectively cancels out its initial deflection in the return path.

For the second issue, let us first calculate the beam shift analytically using the Fourier transforming property of an objective lens. The BFP is related to the image plane by a Fourier transformation. The tilts in the BFP are transformed to shifts in the image plane. We use this property to scan the focused spot across the sample in the image plane. If the galvo mirror is not placed in the BFP conjugate plane, the beam in the



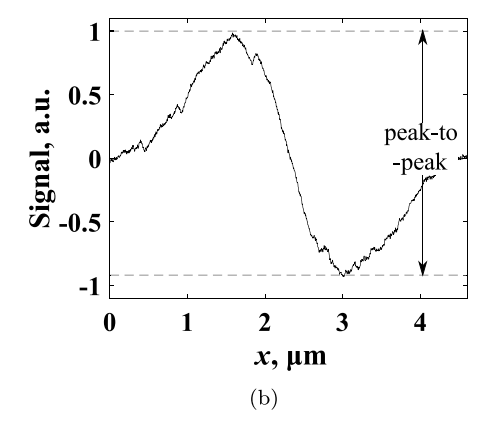


Fig. 2. Typical CFS differential signal: (a) 2D representation of a scan of an etched hole of 425 nm diameter and 60 nm depth etched into Si, (b) cross-section along the x-axis indicated by the black dotted line in (a). The CFS system uses an 0.4 NA objective and 633 nm wavelength.

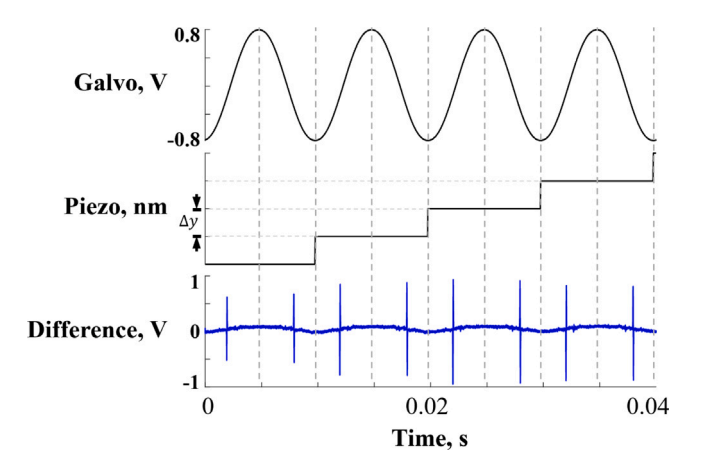


Fig. 3. Voltage signals recorded from multiple channels: Galvo — feedback signal from the galvo mirror (x-axis), Piezo — feedback from the piezo used in the slow axis (y-axis), differential — signal from the split-detector obtained by subtracting the output signals from the two photodiodes and normalised. The dotted lines are used to separate each scan line. The scan parameters used where: galvo frequency — 100 Hz, galvo amplitude — 800 mV, line separation of 100 nm, all signals sampled at 1 MHz. The sample consists of a Si wafer with 400 nm PSL particles.

BFP gets shifted in addition to the tilt from the mirror. The shift at the BFP after extrapolation is calculated to be,

$$\delta = (dz + d\tan\theta)\tan 2\theta,\tag{1}$$

where  $\theta$  is the angle of rotation of the galvo mirror, dz is the distance from the rotational axis of the galvo mirror to the BFP, and d is the distance from the rotational axis to the point of incidence of the beam on the galvo mirror, measured along the optical axis. A schematic of the beam shift is shown in Fig. 4.a. The detailed calculations are included in Appendix A. The beam at the BFP thus has a shift of  $\delta$  and tilt of  $2\theta$  with respect to the optical axis.

At the image plane, in addition to the shift caused by the beam tilt in the BFP, the beam is also tilted by an angle  $\alpha$ , a function of the shift in the BFP. After reflection from the sample, the angle changes from  $\alpha$  to  $-\alpha$ . The field in the BFP, after Fourier transformation, is then shifted by  $-\delta$ .

The lateral shift is de-magnified by lenses L5 and L6, which relays the BFP to the split detector. The beam position at the split-detector is thus shifted if the galvo mirror is shifted from the BFP. When the beam is shifted with respect to the middle of the split-detector, left and right halves of the bi-cell have unequal amounts of light incident on them. The shift thus creates an asymmetry causing the split-detector to act

as a position sensor. Since the shift is a function of the galvo angle, the signal generated due to the shift follows the galvo motion with the same frequency and with an amplitude proportional to  $\delta$ . If g(t) is the signal generated from the beam shift and d(t) is the differential signal from the sample scan. The total output signal s(t) = g(t) + d(t), the contribution from the beam shift, g(t), is minimised when the galvo is in the BFP. Fig. 4.b and Fig. 4.c show the output signal from the split detector when the galvo mirror is placed at the BFP and slightly shifted from the BFP, respectively. Appendix B shows the influence of beam offset on the CFS differential signal.

Furthermore, the shift can also introduce vignetting unless the beam diameter is significantly larger than the exit pupil diameter. However, increasing the beam diameter beyond the exit pupil diameter results in poor utilisation of the laser power.

Thus, we choose the galvo mirror to be placed in a plane conjugate to the BFP of the objective and in a double-pass configuration. This ensures the beam at the split-detector is neither tilted nor shifted. Appendix C details the process of aligning the galvo mirror in the setup experimentally. In the next section, we tackle the more fundamental issue of off-axis aberrations.

# 4. Off-axis aberrations

As the galvo mirror scans the beam through a range of angles, the optical path varies slightly for each angle. Depending on the optical path, the beam experiences different aberrations. To quantify the change in aberrations for different beam angles, we used a Shack-Hartmann wavefront sensor (SHSCam SHR-150-CL, Optocraft) to experimentally measure the amount of optical aberrations in the far field. The aberrations are described using Zernike polynomials. In theory, any general wavefront defined on a circular pupil can be decomposed in terms of Zernike polynomials as [32]:

$$W(\rho,\varphi) = \sum_{nm} C_n^m Z_n^m(\rho,\varphi)$$
 (2)

where,  $C_n^m$  is the coefficient corresponding to each Zernike polynomial  $Z_n^m$  in the decomposition of the general wavefront W. Each polynomial is defined on a unit circle with  $0 \le \rho \le 1$ ,  $0 \le \varphi \le 2\pi$  and

$$Z_n^m(\rho,\varphi) = R_n^m(\rho) \cdot \begin{cases} \cos m\varphi & m \ge 0\\ \sin m\varphi & m < 0 \end{cases}$$
 (3)

The radial function  $R_n^m(\rho)$  is defined as

$$R_n^m(\rho) = \sum_{k=0}^{(n-m)/2} (-1)^k \frac{(n-k)!}{k!(\frac{n+m}{2}-k)!(\frac{n-m}{2}-k)!} \rho^{n-2k} . \tag{4}$$

where, n = 0, 1, 2, etc. is the radial index and m = -n, -n + 2, ..., n - 2, n is the azimuthal index. Aberrations distort the intensity distribution of the focal spot in the image plane, subsequently affecting the differential

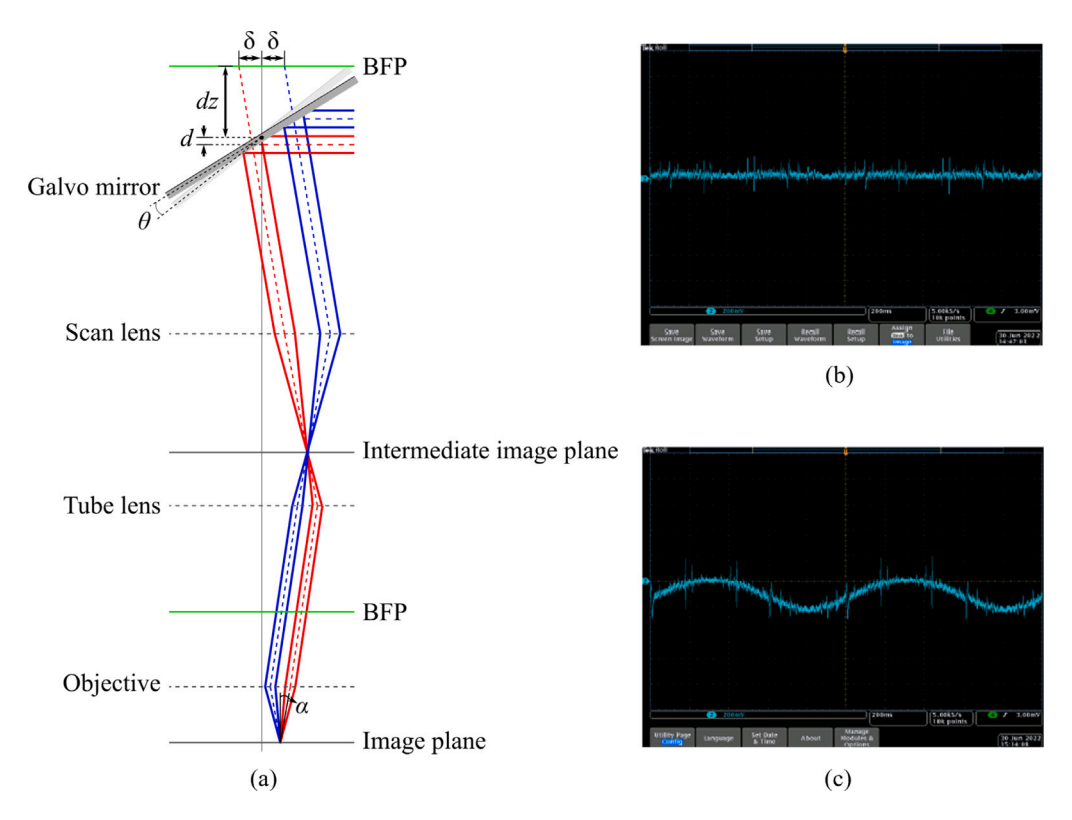


**Fig. 4.** (a) Schematic illustration of a beam shift at the back focal plane (BFP) due to the displacement of the galvo mirror from the ideal BFP position (red — incident beam, blue — reflected beam), where δ is the shift of the beam after reflection w.r.t. the optical axis, dz is the distance between the BFP and the rotational axis of the galvo mirror, d is the distance from the rotational axis to the point of incidence of the beam on the galvo mirror. Screenshot of the differential signal from the split detector while scanning with the galvo mirror (b) positioned exactly at the BFP and (c) shifted by 5 mm from the BFP.

signal recorded in the Fourier plane. Fig. 5 shows the effect of low-order Zernike aberrations on the focus spot and on the CFS signal. For each mode, we show the pupil-phase profile, the resulting intensity distribution at the image plane, and the simulated two-dimensional differential signal for a Si sample with a 400 nm diameter, 150 nm deep etched pit (input field linearly polarised along x in the pupil plane, NA=0.4,  $\lambda$  = 633 nm). The Strehl ratio of the aberrated spot and the peak-to-peak of the differential signal are reported alongside. As expected, the peak-to-peak decreases as the Strehl ratio drops, but the dependence is not linear. A systematic study of mode-dependent influence on the CFS differential signal is presented in Soman et al. (2025) [33].

During the measurements, the beam angle was varied from -10° to +10°. These angles correspond to twice the galvo mirror angles. Beyond this range, the beams suffered from clipping due to the finite aperture size of the scan lens. The aberrations were measured in the back focal plane of the objective before the beam is focused on the sample. For each angle, we looked only at the low-order Zernike aberrations, namely, defocus, spherical, astigmatism, oblique astigmatism, horizontal and vertical coma aberrations. The wavefront sensor measures the coefficient corresponding to each aberration in units of wavelength of the incident light. Fig. 6 shows the plots for the amounts of different aberrations as a function of the beam angle. Astigmatism, oblique astigmatism, and vertical coma exhibit the most variation with the beam angle. This is logical, as one of the primary contributors to astigmatism in an optical system is the presence of off-axis beams. The larger the off-axis angle, the greater the asymmetry in the wavefront, resulting in more pronounced non-axisymmetric aberrations such as astigmatism and coma.

Next, we looked at the combined influence of these aberrations on the peak-to-peak voltage of the differential signal. For this study, the galvo is held fixed at a certain angle using a DC voltage while the sample is scanned using a 2D piezo stage (P-625.2 CD). A 2D scan

map using the piezo stage with the galvo mirror at 0° is shown in Fig. 7.b. The sample consisted of an array of 90 pits etched into a silicon wafer. Each pit has a nominal diameter and etch depth of 200 nm and 60 nm respectively. There might be small variations in the actual values due to the fabrication process. To study the variation in the peak-to-peak voltage as a function of the galvo angle, the peak-to-peak voltages is averaged across all the pits. The scan parameters are: xspeed -  $500 \,\mu\text{m/s}$ ,  $\Delta y$  -  $200 \,\text{nm}$ , sampling rate -  $50 \,\text{kHz}$ . Fig. 7.a shows the variation in the signal peak-to-peak as a function of the galvo angle. The signal peak is highest at 0° and reduces for larger angles. The asymmetry observed around 0° is likely due to a misalignment of one or more components in the optical setup. For angles of  $\pm 1.6^{\circ}$ , the mean signal remains within 90% of the peak value measured at 0°. Beyond these angles, it is advisable to apply post-processing corrections to account for the signal reduction. It is worth mentioning that this range of acceptable angles is determined uniquely for our optical system and may be different depending on the optical components used.

We now have an optical system with specific ranges of scan parameters that have been experimentally defined. The next step is to evaluate the system requirements for high-speed scanning, focusing specifically on the minimum bandwidth needed for the detector to accurately track the optical signal.

# 5. Detection bandwidth

To calculate the minimum detection bandwidth, we need to know what the highest spatial frequency is that our optical system can pass through. Assuming no non-linear interactions between the focus spot and sample, the spatial cutoff frequency can be calculated as [34–36],

$$f_{\text{cutoff}} = \frac{2\text{NA}}{\lambda},\tag{5}$$

where  $\lambda$  is the wavelength of the coherent source and NA is the numerical aperture of the focusing lens. The spatial cutoff frequency

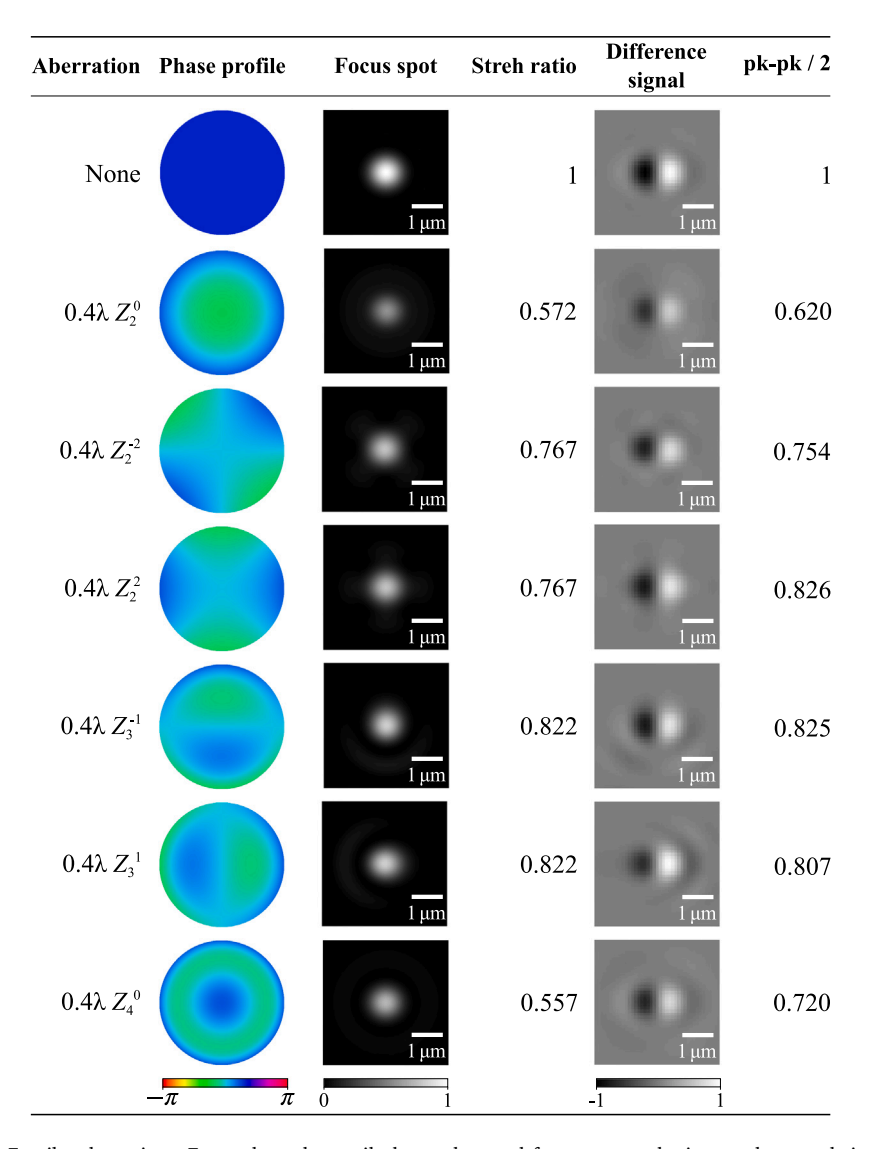


Fig. 5. Influence of low-order Zernike aberrations. For each mode: pupil phase, aberrated focus spot at the image plane, and simulated CFS differential signal for a sub-wavelength structure (pit of 400 nm diameter and 150 nm depth etched in Si). The input field is linearly polarised along x-direction in the pupil,  $\lambda = 633$  nm, NA = 0.4. Reported Strehl ratios correspond to the shown spots. Zernike coefficients are specified as peak-to-valley (PV). The differential signal is quantified using peak-to-peak (pk-pk) values.

is expressed in cycles per spatial unit. The cutoff frequency in Hz depends on the speed at which the spot scans the surface as well as the scanning trajectory determined by the input waveform used to drive the galvo mirror. This in turn determines the minimum detector bandwidth required to record the output signal. A detailed discussion on the bandwidth requirements for both linear and non-linear scanning strategies is included in Appendix D.

For the galvo used in the system, the highest modulation achievable is 1 kHz. Thus for a scan width  $w=100\,\mu\text{m}$ , the minimum bandwidth using the approximation  $\beta f_{\rm galvo}$ , where  $\beta=\pi w f_{\rm cutoff}$  is 397.1 kHz. A bandwidth below this threshold can cause signal distortion and reduce the peak-to-peak amplitude. Fig. 8 shows the peak-to-peak values as a function of the galvo frequency for two detection bandwidths: 10 kHz and 560 kHz. For the low-bandwidth detector (10 kHz), the peak-to-peak signal drops with increasing frequency.

# 6. Application: Calibration of etched circular pits with different diameters

In order to check the performance of the CFS setup with the galvo mirror, we used the setup to create a calibration curve for etched circular pits with varying diameters. The calibration sample consisted of an array of circular pits etched into a Si substrate, with diameters ranging uniformly from 325 nm to 925 nm in 100 nm increments and a constant depth of 60 nm. The pits were spaced  $10\,\mu\text{m}$  apart and fabricated using e-beam lithography followed by dry etching. The measured values of the etched pit diameter and depth are included in Appendix E. The scan parameters were:  $f_{\text{galvo}}$  - 10 Hz,  $\Delta y$  - 200 nm, sampling rate - 1 MHz. The resulting calibration curve, shown in Fig. 9, plots the peak-to-peak signal as a function of the pit diameter. Each data point is an average of 12 independent measurements with a coverage factor of k=1. This curve demonstrates the system's ability to correlate the measured signal with specific pit sizes. The calibration curve can then be used to measure pits of unknown diameters within this range or measure deviations from a nominal diameter value during the manufacturing process.

#### 7. System performance assessment

In CFS, the asymmetry in the far-field generated while scanning a focused spot across a sample is converted from an optical signal to an electronic signal using photo-detectors and amplifying circuits. In

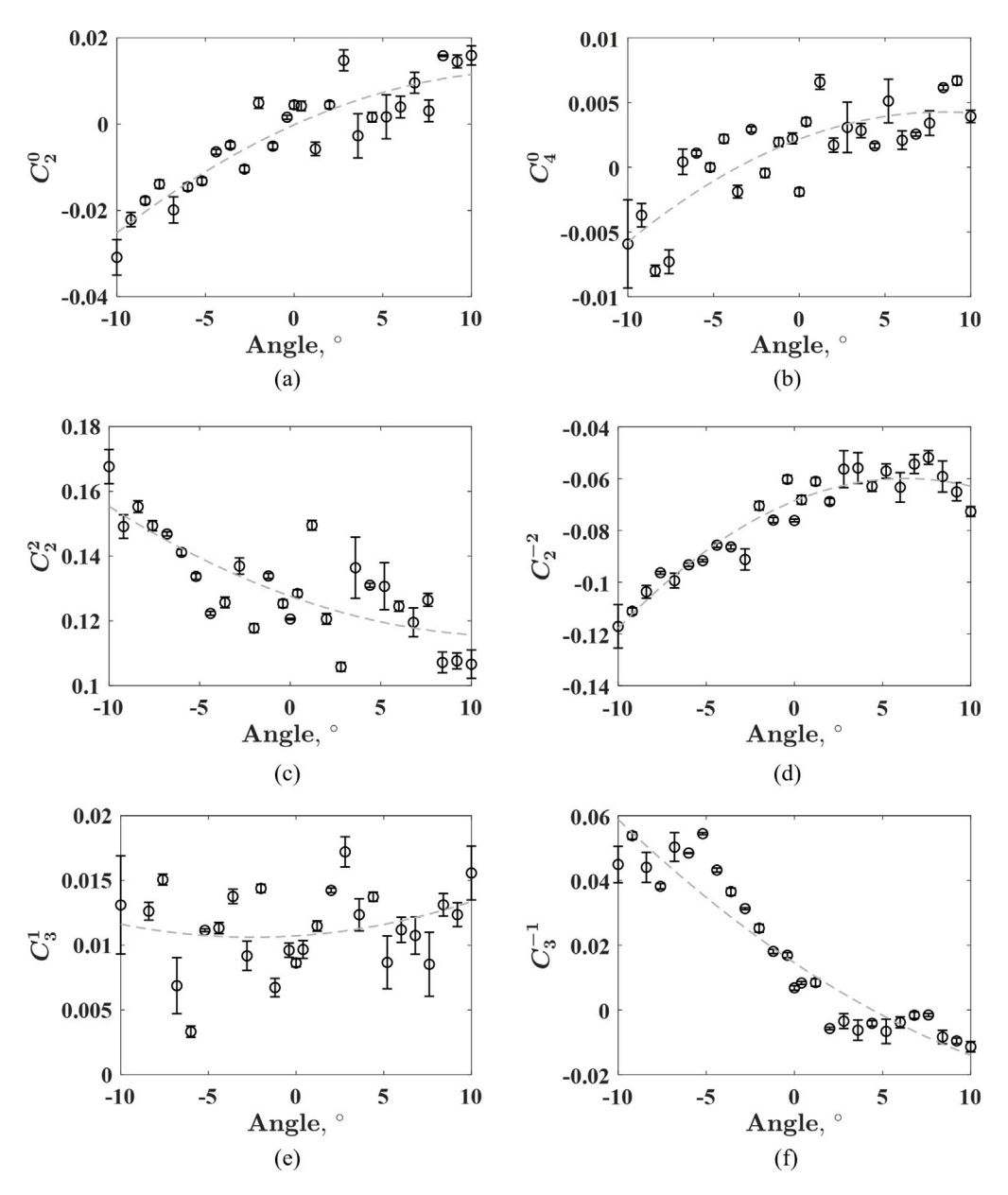


Fig. 6. Zernike coefficients as a function of the beam angle for (a) defocus, (b) spherical, (c) astigmatism, (d) oblique astigmatism, (e) horizontal coma, (f) vertical coma aberrations. The coefficients were measured using a Shack-Hartmann wavefront sensor (SHSCam SHR-150-CL, Optocraft) in the back focal plane. Each datapoint is an average of 5 independent measurements.

earlier sections, we discussed how optical aberrations contribute to measurement uncertainty. In this section we quantify the uncertainty from the aberrations as well as from sources such from the detection circuit and ADC (analog-to-digital converter), laser power fluctuations, substrate surface roughness, galvo repeatability, piezo positioning and sample tilt. All measurements were conducted at a controlled temperature of 21 °C with fluctuations limited to 0.1 °C. The contribution to measurement uncertainty due to the thermal expansion is assumed to be minimal.

# 7.1. Galvo mirror

The scanning performance in terms of linearity and repeatability using the galvo was experimentally determined.

**Linearity**. To obtain the linearity of the galvo system, the beam angle was computed from camera images taken at a known distance. As the beam was scanned, the spot shifted across the camera sensor. Given

the pixel size the angle was obtained using trigonometric relations. Fig. 10(a) shows the beam angle versus input voltage. The data follow the nominal slope of 4 °/V with a high  $R^2=0.9998$ . The linearity of the focus spot shift versus beam angle was measured using a fabricated ruler sample comprising 200 nm diameter, 150 nm deep pits on a 10  $\mu$ m pitch etched in silicon (Si). Fig. 10(b) shows the computed spot shift as a function of beam angle (limited to the predetermined scan range). The relation is linear with a slope of  $40.98\,\mu$ m/° and  $R^2=0.9998$ .

Repeatability. The repeatability of the scan measurements using a galvo mirror was measured by repeatedly scanning a line across a particle smaller than the focus spot. The focus spot was first centred on the particle and several line scans were made using the galvo mirror. The peak-to-peak of the output signal from the line scan was computed for each measurement. Any wobble or other galvo errors causes deviations in the peak-to-peak signal. Fig. 11 shows variation in signal peak-to-peak across 190 measurements. The measurements are centred around a mean value of 0.2086 V with a standard deviation

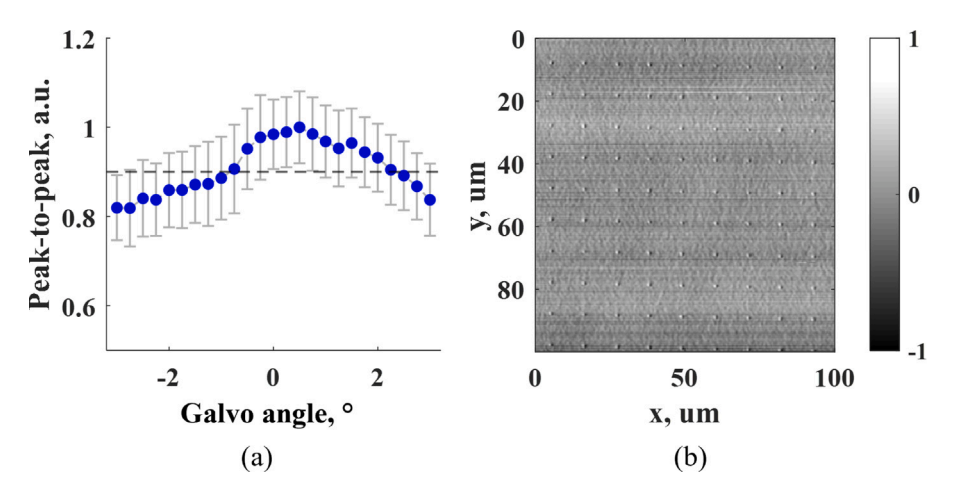
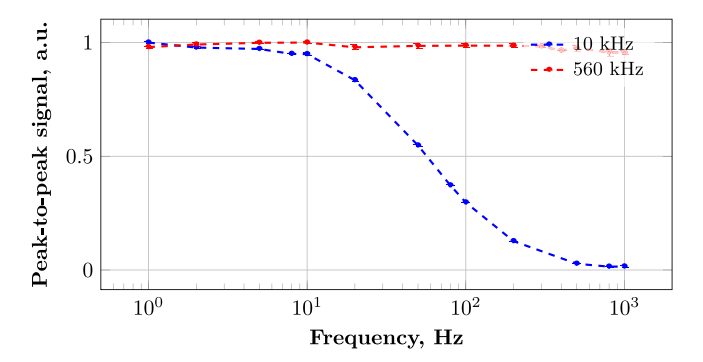


Fig. 7. (a) Peak-to-peak of the differential signal from the split-detector corresponding to the detection of one pit plotted as a function of galvo mirror angle. (b) The 2D differential scattering map, obtained using a 2D piezo stage, of an array of circular pits of 200 nm diameter and etched to a depth of 60 nm in Silicon at a galvo angle of 0°. Each data point in (a) is an average of the peak-to-peaks for the entire array with each pit measured twice.



**Fig. 8.** Peak-to-peak signal amplitude as a function of galvo frequency for detectors with bandwidths of 10 kHz and 560 kHz. The peak-to-peak drops significantly using the low-bandwidth detector. Each data point is an average of 12 independent measurements with a coverage factor of k = 1.

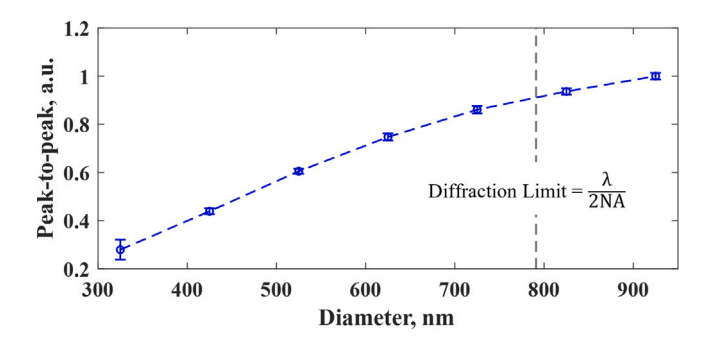
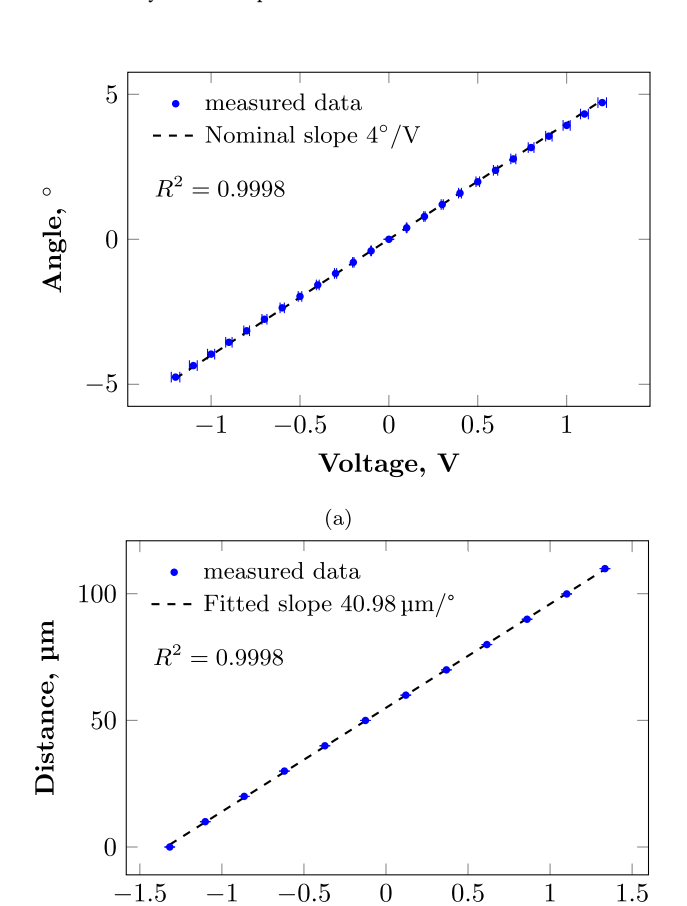


Fig. 9. Peak-to-peak of the differential signal from the split-detector plotted as a function of the etched hole diameter. The system uses an  $0.4~\mathrm{NA}$  objective and laser source of  $633~\mathrm{nm}$ .

of  $2.78\,\mathrm{mV}$  leading to a coefficient of variation of 1.34% or relative measurement uncertainty of 0.0134.

**Lateral resolution.** The optical resolution is determined by the parameters such as the NA of the objective and wavelength,  $\lambda$ . Using the spatial frequency cutoff as a measure for the spatial resolution, the largest measurable spatial frequency is  $2NA/\lambda$ . The minimum resolution needed to satisfy the Nyquist sampling requirement is thus,

$$\Delta_{\text{Nyq}} \le \frac{1}{2f_c} = \frac{\lambda}{4 \, \text{NA}}.$$



**Fig. 10.** Experimental evaluation of galvo mirror linearity. (a) Beam angle versus input voltage: measurements (blue markers) closely follow the nominal  $4 \,^{\circ} \, V^{-1}$  response slope (dashed), with  $R^2 = 0.9998$ , (b) Focus-spot displacement versus beam angle: measurements (blue markers) and linear fit (dashed) with a slope of  $40.98 \, \mu m/^{\circ}$ , with  $R^2 = 0.9998$ .

(b)

Angle, °

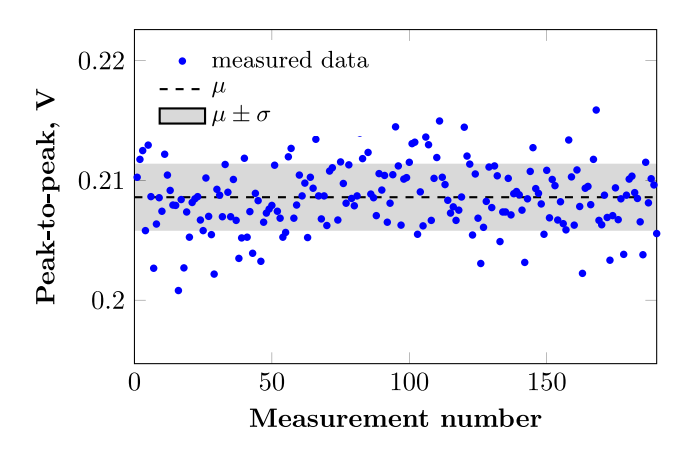


**Fig. 11.** Repeatability of galvo-mirror line scanning. Peak-to-peak signal from 190 repeated measurements. Points (blue circles) are individual measurements; the dashed line marks the mean,  $\mu=0.2086\,\mathrm{V}$ ; the shaded band shows  $\mu\pm\sigma$  with  $\sigma=2.78\,\mathrm{mV}$ . The coefficient of variation is 1.34%.

For  $\lambda=633\,\mathrm{nm}$  and NA = 0.4, this gives  $\Delta_{\mathrm{Nyq}}\approx0.396\,\mu\mathrm{m}$ . Along x (galvo axis), the small-angle spot shift is linear with angle at  $40.98\,\mu\mathrm{m}/^\circ$  (measured). Using the specification of the galvo mirror from the manufacturers, the resolution in angle is  $0.000\,86^\circ$ , the minimum lateral resolution achievable using the system is thus  $0.035\,\mu\mathrm{m}$ . The minimum resolution satisfying the Nyquist resolution is much higher than the resolution achievable using the current scan system. In other words, lateral sampling is comfortably finer than required by the optical resolution. The instrument is optics-limited, not actuator-limited, along both axes.

# 7.2. Aberration

Within the scan range  $\Theta \in [-A,A]$  with  $A=1.6^\circ$ , determined in Section 4, the measured dependence of the differentia-signal peak-to-peak on scan angle, shown in Fig. 7, is fit using a third order polynomial.

$$y = \frac{V_{\text{pp}}(\theta)}{V_{\text{pp}}(0)} = 1 - b\theta^2 + c\theta^3, \qquad b = 0.0421, \ c = 0.0094,$$
 (6)

where  $\theta$  is in degrees and  $R^2 = 0.9533$ . We model the scan angle as uniformly distributed,  $\Theta \sim U[-A,A]$  with

$$\mu_{\Theta} = \mathbb{E}[\Theta] = 0, \quad \operatorname{Var}[\Theta] = \mathbb{E}[\Theta^2] = \frac{A^2}{3}, \quad \mathbb{E}[\Theta^4] = \frac{A^4}{5}, \quad \mathbb{E}[\Theta^6] = \frac{A^6}{7},$$

(7)

and all odd moments  $\mathbb{E}[\Theta^{2k+1}] = 0$  by symmetry. To compute the uncertainty of the measurement, the value of the fit at the measurement average of  $\theta$  is calculated,

$$y \Big|_{\mu_{\Theta}=0} = 1$$
,  $\frac{\partial y}{\partial \theta} \Big|_{\mu_{\Theta}=0} = 0$ ,  $\frac{\partial^2 y}{\partial \theta^2} \Big|_{\mu_{\Theta}=0} = -2b$ ,  $\frac{\partial^3 y}{\partial \theta^3} \Big|_{\mu_{\Theta}=0} = 6c$ . (8)

In most cases, the first order variance is sufficient to compute the uncertainty. However since the first derivative,  $\frac{\partial y}{\partial \theta} = 0$ , higher order terms should be considered [37]. For  $Y = V_{pp}(\Theta)/V_{pp}(0)$ ,

$$\operatorname{Var}[Y] = -\frac{1}{4} (\operatorname{Var}[\Theta])^2 \left( \frac{\partial^2 y}{\partial \theta^2} \right)^2 + \frac{1}{4} \mathbb{E}[\Theta^4] \left( \frac{\partial^2 y}{\partial \theta^2} \right)^2 + \frac{1}{36} \mathbb{E}[\Theta^6] \left( \frac{\partial^3 y}{\partial \theta^3} \right)^2$$
(9)

$$=b^2 A^4 \frac{4}{45} + c^2 \frac{A^6}{7},\tag{10}$$

$$=0.001244$$
 (11)

$$=u^2(\theta) \tag{12}$$

where,  $u(\theta)$  is the relative measurement uncertainty. For  $V_{\rm pp}(0)=1~{\rm V}$ , the measurement uncertainty is  $0.0353~{\rm V}$ .

#### 7.3. Sample tilt

The effect of sample tilt is essentially that of defocus aberration with the variation in signal peak-to-peak following the curve shown in Appendix F. The effect is minimised by following a sample mounting protocol detailed in Appendix C. This should ensure that the sample is flat to within half a wavelength. To account for sample drift, the effect of shift of  $\pm 1\lambda$  can be calculated. The data close to the best focus  $\pm 1\lambda$ , shown in Fig. F.18, is fitted with a second order polynomial,

$$y = \frac{V_{\rm pp}(0)}{V_{\rm pp}(z)} = 1 - bz^2, \quad b = 0.0417,$$
 (13)

where z=0 corresponds to the plane with the highest peak-to-peak. The axial shift, z is modelled to be normally distributed,  $Z \sim (0, \lambda)$ . Following the same procedure as earlier and using the second order variance.

$$u^{2}(z) = \frac{\sigma^{4}}{2} \left(\frac{\partial^{2} y}{\partial z^{2}}\right)^{2},\tag{14}$$

$$=0.00055$$
 (15)

The measurement uncertainty corresponding to a maximum  $V_{\rm pp}=1\,{\rm V}$  is 0.0236 V.

#### 7.4. Detector

The uncertainty contribution from the detector is from the ADC as well as the photodiodes. The noise from the ADC can be classified into two parts: quantisation and thermal noise. The root mean square (RMS) quantisation noise is  $8.8\,\mu V$  [38]. The RMS value of the thermal noise measured by shorting the input channels is  $197.6\,\mu V$ . The noise from the detector measured when no light is incident on the photodiodes is  $881.4\,\mu V$ , given a measured detection bandwidth of 560 kHz.

#### 7.5. Laser

The peak-to-peak of the differential signal varies linearly as a function of input laser power. Any fluctuations in the laser intensity can thus directly influence the output signal. The HeNe laser has low-frequency power fluctuations and has minimal influence if the measurement lasts only for a few seconds. However, for longer measurements using an intensity-stabilised laser would be preferred. The RMS noise contribution due to the laser fluctuation for a 5 min measurement is 1.342 mV. The measurement is done 2 h after the laser is switched on and the power at the sample was  $68\,\mu\text{W}$ .

#### 7.6. Piezo

The z-piezo is used for positioning the sample in the right plane to get the maximum peak-to-peak signal. The peak-to-peak drops as a function of distance from the optimal plane (see Appendix F). Positioning inaccuracies of the piezo system can lead to shift of the sample position from this optimal measurement plane contributing to measurement uncertainties. The positioning error for the z-stage was measured using the built-in sensor used for closed-loop feedback. The standard deviation of the positioning error set at half its travel range, i.e. 19  $\mu m$  is 0.11 nm. The effect of such a small displacement cannot be measured experimentally using the current setup. The contribution to the measurement uncertainty from the z-stage can thus be entirely neglected.

 $\label{eq:table 2} \textbf{Uncertainty budget entries. All uncertainties to be combined in quadrature.} \\ \textbf{The uncertainties correspond to a measured differential signal of 1 $V_{pp}$.}$ 

			**
Source	Uncertainty type [40]	Distribution	Uncertainty in V
ADC	A	Normal	$1.97 \times 10^{-4} \text{ V}$
Detector	A	Normal	$8.81 \times 10^{-4} \text{ V}$
Laser	A	Normal	$1.34 \times 10^{-3} \text{ V}$
Galvo	A	Normal	0.0134 V
Aberration	В	Model	0.0353 V
Sample tilt	В	Model	0.0236 V
Surface roughness	A	Normal	$1.605 \times 10^{-3} \text{ V}$

**Table 3**Galvo-based fast axis (sinusoidal drive) versus piezo-stage key parameters under identical optics. Detector bandwidth entries are the measured 99% energy cutoffs.

Metric	Scanning strategies		
	Galvo (GVS211/M)	Piezo (P-625.2 CD)	
Scan trajectory	Sinusoidal	Triangular	
Scan range	$130  \mu m \times 500  \mu m$	$500  \mu m \times 500  \mu m$	
Scan speed	1 kHz	3 Hz <sup>a</sup>	
Minimum pixel size	35 nm	1.4 nm	
Bandwidth for 99% power	~397.1 kHz	~6.4 kHz	
Numerical aperture (NA)	0.4	0.4	
Laser wavelength	633 nm	633 nm	
Laser power at sample	68 μW	68 μW	
Measurement uncertainty <sup>b</sup>	44.54 mV	23.63 mV	
Throughput <sup>d</sup>	1 s	5 min <sup>e</sup>	

- <sup>a</sup> 1/35 of the first resonant frequency of the piezo (P-625.2 CD).
- $^{\rm b}$  1  $\sigma$  measured at 1  $\rm V_{pp}.$  Does not include surface roughness.
- <sup>c</sup> Polystyrene latex (PSL) particle diameter.
- $^d$  Area of  $100\,\mu m \times 100\,\mu m$  with a pixel size of  $100\,nm$
- e @ 3 Hz scan frequency.

#### 7.7. Surface roughness

Surface roughness does not contribute to the noise floor of the detection but it does raise the background signal level considerably. Especially for particle detection, it often limits the size of the smallest detectable particle [39]. For a blank single-side polished Si wafer with  $h_{\rm RMS} < 0.5$  nm, the RMS value for the differential signal is 1.605 mV.

The above error sources, with the exception of surface roughness, are both uncorrelated and sample-independent. Sample roughness varies with the sample and cannot be generalised. Table 2 lists the different error sources for a measured differential signal with 1  $V_{\rm np}$ .

#### 8. Conclusion

In this paper, we have proposed a new beam scanning CFS setup using a 1D galvo mirror for fast metrology applications. The influence of the position of the mirror with respect to the Fourier plane is studied. The effect of beam angle on the peak-to-peak signal from a sub-wavelength nanostructure is analysed. Aberrations reduce signal peak-to-peak and can also distort the optical impulse response of the system. Off-axis beams are more aberrated compared to the on-axis beams. In practice, this limits the range of angles that can be used for scanning. In our setup using a 0.4 NA objective, the signal peak-to-peak drops to 90% for galvo angles  $\pm 1.6^{\circ}$ .

The split-detector used in the experiment consists of a bi-cell which is used to record the differential signal between the two diodes. Considering the bandwidth scaling with scanning frequency, the maximum speed with which the sample can be scanned appears to be limited by the detector bandwidth. The relation between the galvo frequency and the corresponding minimum detection bandwidth is calculated. In this work, we demonstrated the beam-scanning setup using a 1 kHz galvo mirror using a detector with a bandwidth of 560 kHz.

In previous CFS setups using piezo-based scanning stages for both the x and y axes, the scan time per line of  $100\,\mu\text{m}$  is 300 ms. The total scan time for scanning an area of  $100\,\mu\text{m} \times 100\,\mu\text{m}$  with steps of  $0.1\,\mu\text{m}$  in the y-direction is 5 min. Using a galvo mirror for the same scan parameters the scan time reduces to 1 s. Table 3 compares the key parameters of the CFS setups using galvo-based scanning versus piezo-based scanning. This architecture maps naturally to roll-to-roll manufacturing, where the moving web provides the slow scan axis and the galvo performs the fast-axis beam scan, enabling continuous inline inspection [41]. The setup can be modified to use dual axis galvo mirrors to enable beam scanning in two directions while the sample is kept fixed. Finally, the low power (68  $\mu$ W) on the sample along with the fast scanning makes the galvo-based CFS system a versatile metrology tool which can be used for the inspection or characterisation of nanostructures.

#### CRediT authorship contribution statement

Sarika Soman: Writing – original draft, Visualization, Validation, Methodology, Investigation. Roland C. Horsten: Writing – review & editing, Software, Data curation. Silvania F. Pereira: Writing – review & editing, Supervision, Project administration, Funding acquisition, Conceptualization.

#### Declaration of competing interest

The authors declare the following financial interests/personal relationships which may be considered as potential competing interests: Silvania F. Pereira reports financial support was provided by Dutch Research Council. If there are other authors, they declare that they have no known competing financial interests or personal relationships that could have appeared to influence the work reported in this paper.

#### Acknowledgements

We acknowledge the Nederlandse Organisatie voor Wetenschappelijk Onderzoek (Project 17–24 Synoptics No. 2) and the Project 20IND09 "PowerElec" within the Program EMPIR, which is jointly supported by the European Commission and the participating countries within the European Association of National Metrology Institutes (EU-RAMET), Germany for funding this research. We also thank Thomas Scholte for his help designing and building optical components while building the setup and Abdelouahid Boujnane from SETTELS for the discussion on optical design.

# Appendix A. Beam shift calculation

In this section, the beam shift after the galvo reflection is calculated in the exit pupil plane. This plane is chosen since the pupil plane can be related with ease to the image plane or the sample plane using a simple Fourier transform.

Let the rotation axis of the galvo mirror be shifted from the back focal plane (BFP) by dz. Further, let the incident beam be shifted by d from the mirror rotational axis. Fig. A.12 shows the diagram of the galvo mirror scan including the incident and reflected beams. LM represents the galvo mirror rotated about the rotational axis by an arbitrary amount  $\theta$  and L'M' the unrotated galvo mirror with the mirror tilted by  $45^{\circ}$  with respect to the optical axis. UV and UV' represent the incident beam when the mirror is rotated and unrotated respectively. VW and V'W' are the corresponding reflected beams. The shift is calculated by extending the beams to the BFP. The two reflected beams intersect the BFP at C and B respectively. VN is the mirror normal at the point of incidence of the beam. The angle of incidence,  $\angle$ UVN, and the angle of reflection,  $\angle$ NVW can be calculated from simple trigonometric relations to be  $45^{\circ}$  –  $\theta$ . AS is the normal to the BFP drawn through the rotational axis of the galvo mirror.

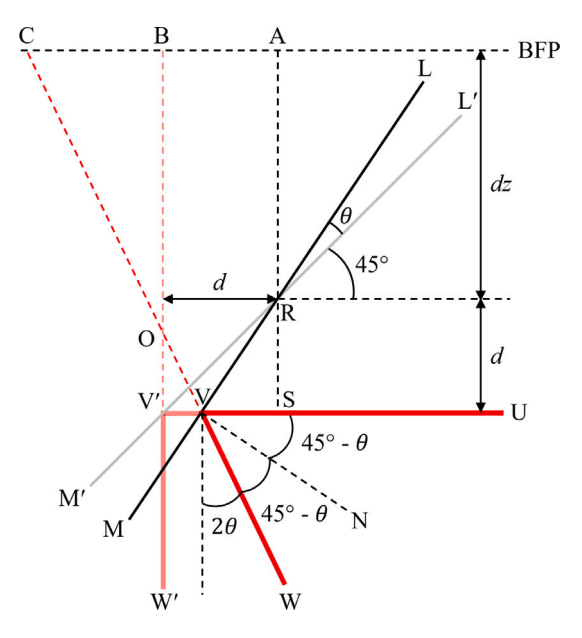


Fig. A.12. Galvo mirror shifted from the exit pupil by dz.

Consider the triangles  $\triangle$  RVS and  $\triangle$  RV'S:  $\angle$ RV'S = 45°,  $\angle$ RVS = 45° +  $\theta$ , and  $\angle$ VRS = 45° -  $\theta$ .

$$VV' = V'S - VS$$

$$= d - \frac{d}{\tan 45^{\circ} + \theta}$$

$$= \frac{2d \tan \theta}{1 + \tan \theta}$$

Now consider the triangles formed by the two reflected beams,  $\triangle$  OVV' and  $\triangle$  OCB.  $\angle$ OV'V =  $\angle$ OBC = 90°,  $\angle$ OVV' =  $\angle$ OCB = 90° – 2 $\theta$ , and  $\angle$ V'OV =  $\angle$ COB = 2 $\theta$ .

$$\mathbf{BV'} = d + dz$$

$$\mathbf{OV'} = \frac{\mathbf{VV'}}{\tan 2\theta}$$

$$= d(1 - \tan \theta)$$

$$\mathbf{OB} = \mathbf{BV'} - \mathbf{OV'}$$

$$= dz + d \tan \theta$$

$$\mathbf{BC} = \mathbf{OB} \tan 2\theta$$

$$= (dz + d \tan \theta) \tan 2\theta$$

Thus the total shift,  $\delta = (dz + d\tan\theta)\tan 2\theta$ . The BFP is related to the image plane by Fourier transform [42]. The beam tilt translates to shift of the focused spot in the image plane and vice versa. Let  $(x_o, z_o)$  be the coordinates in the BFP,  $(x_i, z_i)$  be the coordinates in the image plane and f be the focal length of the Fourier transforming lens. If  $U(x_o)$  is the field in the BFP, the field in the image plane is calculated as,

$$U(x_i) = \frac{1}{j\lambda f} \int_{-\infty}^{\infty} U(x_o) \exp\left[-j\frac{2\pi}{\lambda f}x_i x_o\right] dx_o. \tag{A.1}$$

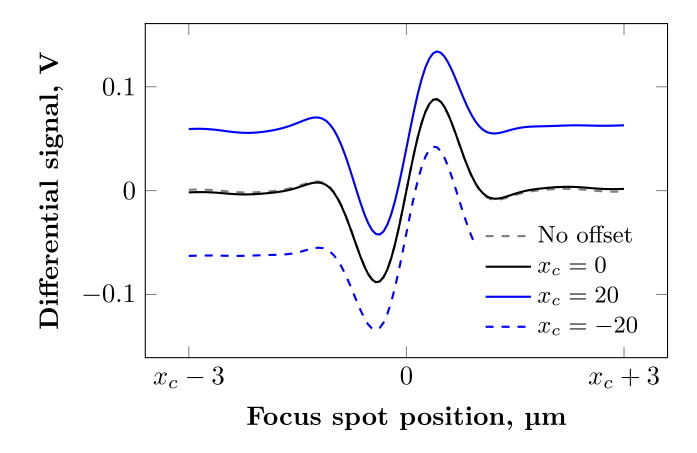
The shifted beam can be denoted as  $U(x_o - \delta)$ , where  $\delta = |\mathbf{BC}|$ . The tilted focused spot at the image plane is,

$$U(x_i) = \exp\left[-j\frac{2\pi}{\lambda f}\delta x_i\right] \mathcal{F}\{U(x_o)\}(x_i)$$
(A.2)

The field after reflection from the image plane is,

$$U(x_i) = \exp\left[j\frac{2\pi}{\lambda f}\delta x_i\right] \mathcal{F}\{U(x_o)\}(x_i)$$
(A.3)

The reflected field is again Fourier transformed by the same lens. The field at the BFP after reflection is  $U(-x_o + \delta)$ . Thus the shift after reflection from the sample remains the same but flipped about the rotation axis.



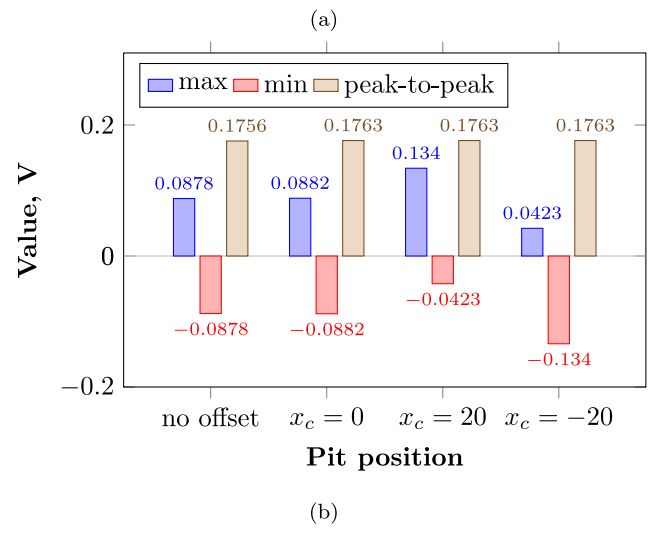


**Fig. B.13.** (a) Differential signals for an etched pit centred at different lateral positions: 0 and  $\pm 20\,\mu m$ . (b) The maximum, minimum and peak-to-peak of the differential signals for different positions.

# Appendix B. Influence of beam offset on the differential signal

To assess impact during scanning over features, we simulated a 400 nm diameter, 150 nm deep pit (NA 0.4,  $\lambda=633$  nm) at three lateral positions ( $x_c=0$  µm and  $\pm 20$  µm) and compared the differential signal over the scan range  $x\in [x_c-3$  µm,  $x_c+3$  µm], shown in Fig. B.13(a). All simulations were carried out with the commercial FDTD solver, Lumerical. The offset changes the shape of the differential signal, making it more asymmetric with unequal peak and valley values. The degree of asymmetry depends on the position of the scatterer within the scan. The peak-to-peak values, however, remain almost the same. Fig. B.13(b) shows the maximum, minimum, and peak-to-peak values of the differential signals for the different pit positions. The peak-to-peak of the scans with offset differs from the scans without offset by 0.39%.

To summarise, offsets do introduce asymmetry in the differential signal. The signal shape or symmetry is very sensitive to small misalignments and also depends on the position of the scattering object within the scan line, but the peak-to-peak of the differential signal is quite robust.

#### Appendix C. Alignment protocols

#### C.1. Galvo mirror

The alignment procedure of the galvo mirror in the BFP is shown in Fig. C.14.

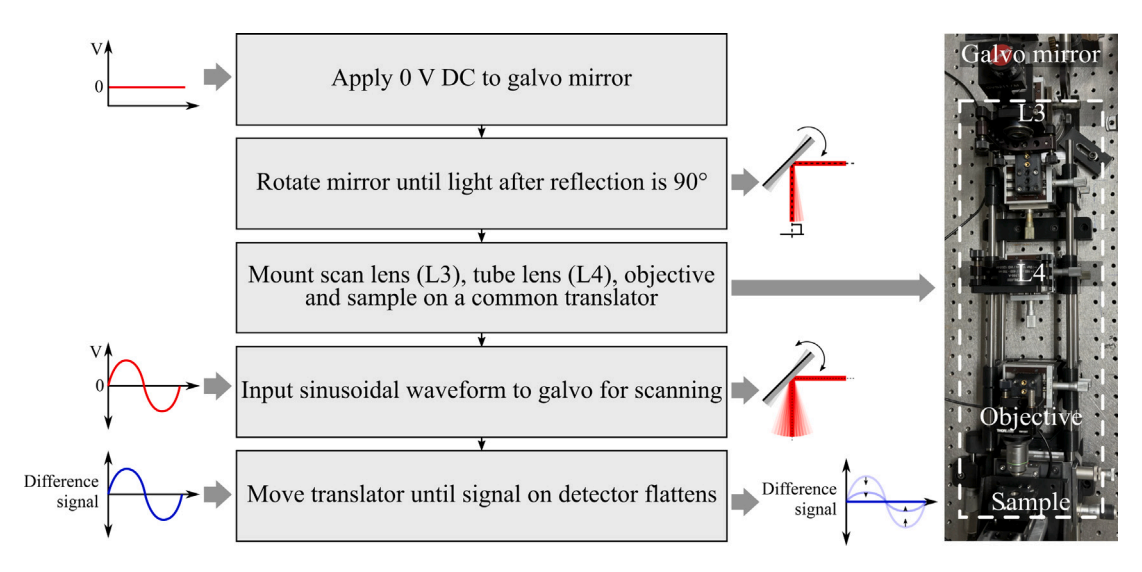


Fig. C.14. Flowchart for aligning the galvo mirror in the Fourier plane.

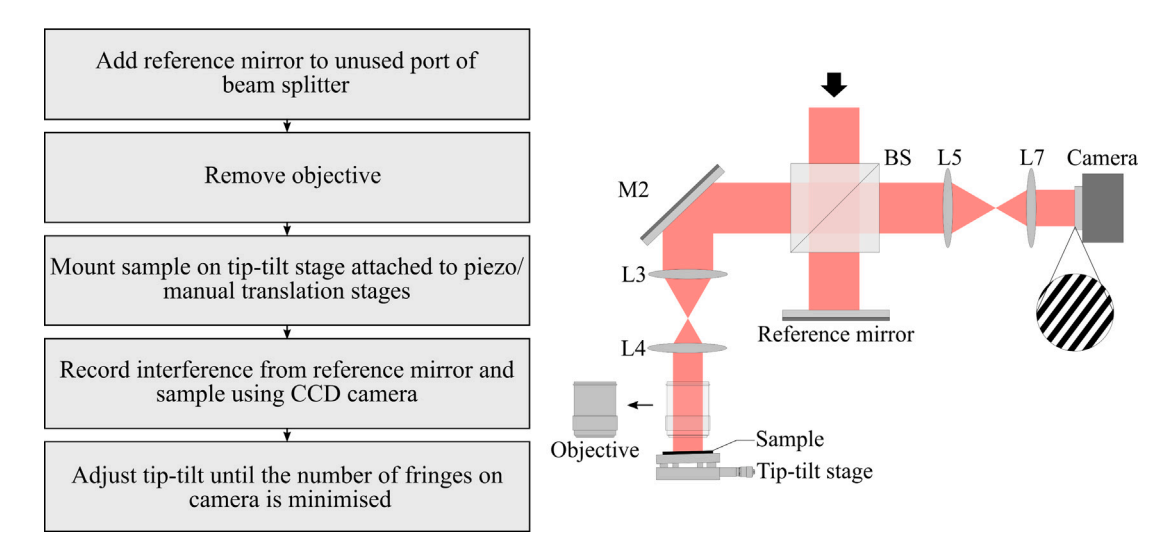


Fig. C.15. Flowchart for minimising sample tilt.

# C.2. Sample

The sample tilt is minimised following the alignment steps shown in Fig. C.15.

# Appendix D. Detection bandwidth dependence on the scanning waveform

Let the sample be a one-dimensional grating with period  $1/f_{\rm cutoff}$ and the differential signal at a position x be,

$$s(x) = \frac{V_{pp}}{2} \sin\left(2\pi f_{\text{cutoff}} x\right),\tag{D.1}$$

where  $V_{pp}$  is the peak-to-peak of the differential signal. With a scan trajectory x = g(t), the measured time signal is,

$$s'(t) = s(g(t)) = \frac{V_{pp}}{2} \sin\left(2\pi f_{\text{cutoff}} g(t)\right). \tag{D.2}$$

The frequency content of the signal can be computed by taking the Fourier transform of the time domain signal [43].

$$\mathcal{F}\{s'(t)\}(f) = S'(f) \tag{D.3}$$

For band-limited spectrum, the detection bandwidth can be determined based on the largest frequency content present. For non-band limited spectrum, a good strategy would be to choose the detector bandwidth that covers 99% of the power. Let us consider a few examples of different scanning strategies but with uniform sampling in the time domain. The optical system in all cases uses a wavelength of 633 nm and an objective of 0.4 NA. The optical cutoff frequency,  $f_{\text{cutoff}} = 1.264$ cycles/μm.

Constant linear velocity: x = vt, where v is the velocity,

$$s'(t) = \frac{V_{pp}}{2} \sin \left(2\pi f_{\text{cutoff}} vt\right). \tag{D.4}$$
  
$$S(f) = \frac{1}{2i} \left[\delta(f - vf_{\text{cutoff}}) + \delta(f + vf_{\text{cutoff}})\right] \tag{D.5}$$

$$S(f) = \frac{1}{2i} \left[ \delta(f - v f_{\text{cutoff}}) + \delta(f + v f_{\text{cutoff}}) \right]$$
 (D.5)

The largest signal frequency is  $|v|f_{\text{cutoff}}$ . Fig. D.16(a) shows the simulated differential scan signal for a grating with period,  $1/f_{\rm cutoff}$  measured with a constant scan velocity,  $v = 300 \,\mu\text{m/s}$ . The corresponding frequency spectrum is shown in Fig. D.16(b). The spectrum is band-limited with the highest frequency peak at 379.2 Hz.

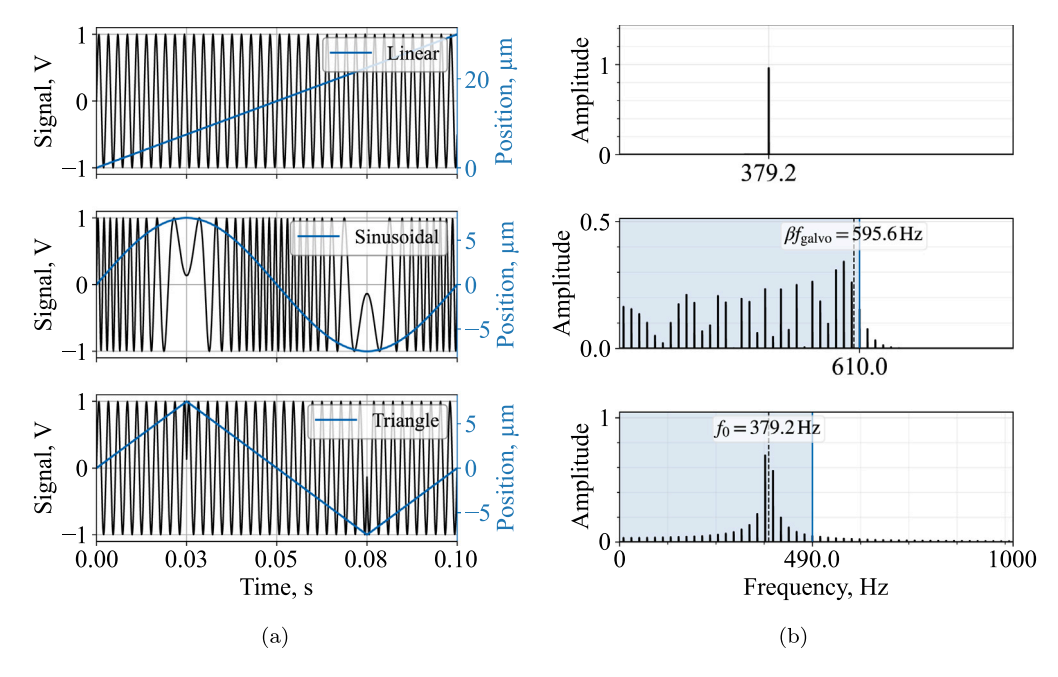


Fig. D.16. Effect of scanning strategies on the measured differential signal and its spectrum. (a) Time-domain signals s'(t) (black, left axis) with the corresponding scan position x(t) (blue, right axis) for constant linear velocity, sinusoidal, and triangular trajectories. (b) One-sided amplitude spectra |S'(f)| for the same cases. Parameters:  $\lambda = 633$  nm, NA = 0.4,  $f_{\text{cutoff}} = 1.264$  cycles/μm;  $f_{\text{galvo}} = 10$  Hz, w = 15 μm, and (linear) v = 300 μm s<sup>-1</sup>. The linear/triangular scans concentrate the power near  $f_0 = v f_{\text{cutoff}} = 379.2$  Hz; the sinusoidal scan produces odd harmonics of  $f_{\text{galvo}}$  with most of the energy within  $\beta f_{\text{galvo}} = 595.6$  Hz,  $\beta = \pi w f_{\text{cutoff}}$ . In (b), the shaded region marks the area below which 99% of the spectral power is contained. Dashed markers indicate  $\beta f_{\text{galvo}}$  (sinusoid) and  $f_0$  (triangle).

**Sinusoidal scanning:**  $x = \frac{w}{2} \sin \left(2\pi f_{\rm galvo} t\right)$ , where, w is the total scan width,  $f_{\rm galvo}$  is the scan frequency of the galvo mirror in Hz,

$$s'(t) = \frac{V_{pp}}{2} \sin \left[ 2\pi f_{\text{cutoff}} \left( \frac{w}{2} \sin (2\pi f_{\text{galvo}} t) \right) \right]$$
 (D.6)

$$= \frac{V_{pp}}{2} \sin \left(\beta \sin(2\pi f_{galvo}t)\right), \quad \beta = \pi w f_{cutoff},$$
(D.7)

$$= \frac{V_{pp}}{2} \left[ 2 \sum_{n=1}^{\infty} J_{2n-1}(\beta) \sin \left( (2n-1) 2\pi f_{galvo} t \right) \right]$$
 (D.8)

The signal expression is expanded using Jacobi-Anger expansion. The signal spectrum can be computed by taking the Fourier transform,

$$S'(f) = \frac{V_{pp}}{2i} \left[ \sum_{n=1}^{\infty} J_{2n-1}(\beta) \left[ \delta(f - (2n-1)f_{galvo}) + \delta(f + (2n-1)f_{galvo}) \right] \right]. \tag{D.9}$$

The spectrum contains only the odd-harmonics of  $f_{\rm galvo}$  with the magnitude determined by  $J_{(2n-1)}(\beta)$ . For a quick approximation, the required detection bandwidth  $\approx \beta f_{\rm galvo} = \pi w f_{\rm cutoff} f_{\rm galvo}$ , as the values of  $J_{(2n-1)}(\beta)$  decay rapidly after  $2n-1>\beta$ . Fig. D.16(a) shows the differential signal acquired during one period of the galvo scan using a sinusoidal input with  $f_{\rm galvo}=10\,{\rm Hz},\,w=15\,{\rm \mu m}$ . Fig. D.16(b) shows the corresponding frequency spectrum:  $\beta f_{\rm galvo}=595.6\,{\rm Hz},\,99\%$  of the power in the spectrum is contained in the frequencies  $\leq 610\,{\rm Hz}$ .

**Triangular scanning:**  $x(t) = \frac{w}{\pi} \arcsin(\sin 2\pi f_{\text{galvo}} t)$ . The time signal is

$$s'(t) = \frac{V_{\rm pp}}{2} \sin \left[ 2w f_{\rm cutoff} \left( \arcsin(\sin 2\pi f_{\rm galvo} t) \right) \right]. \tag{D.10}$$

A triangular scan moves at constant speed on each half-period and reverses at the turning points. The turnarounds (slope reversals every  $2/f_{\rm galvo}$ ) impose a periodic phase discontinuity that generates a line comb around  $f_0=2wf_{\rm galvo}f_{\rm cutoff}$  at odd multiples of  $f_{\rm galvo}$ . For the scan parameters,  $w=15\,\mu{\rm m},~f_{\rm galvo}=10\,{\rm Hz},$  a detector bandwidth of  $f=490\,{\rm Hz}$  captures  $\geq 99\%$  of the signal power. Fig. D.16 shows the differential signal generated when scanning using a triangular waveform as well as the corresponding frequency spectrum. For a quick

**Table E.4**Nominal and measured pit diameters. The diameters were measured using SEM (FEI Helios G4 CX).

Measured diameter (nm)
325.2
424.2
528.8
624.4
709.2
814.9
917.3

rule of thumb calculation, using  $f_0 + c f_{\rm galvo}$ , where  $c \approx 5-10$  should suffice. Smoothening the turnarounds will reduce the energy in the sidebands, lowering the required bandwidth.

A sinusoidal waveform thus puts higher requirements on the detection bandwidth compared to the linear strategies.

# Appendix E. Sample measurements

The pit diameter was measured using SEM (FEI Helios G4 CX) and the etch depth was measured using white light interferometer (ContourX-500). Fig. E.17 shows the sample measurements: SEM images of the diameter of the pits and height profile obtained using the white light interferometer. The measured diameters values are listed in Table E.4. The average deviation from the nominal value is  $5.9\,\mathrm{nm}$ . The measured etch depth is  $59.3(8)\,\mathrm{nm}$ .

# Appendix F. Influence of the out-of-focus position (z -axis)

The peak-to-peak of the differential signal is influenced by the axial position of the sample. Fig. F.18 plots the reduction in the peak-to-peak as a function of the axial position of the sample. The sample used for the measurement consists of a pit with nominal diameter and etch depth of 1025 nm and 60 nm respectively, etched into a Silicon wafer. From

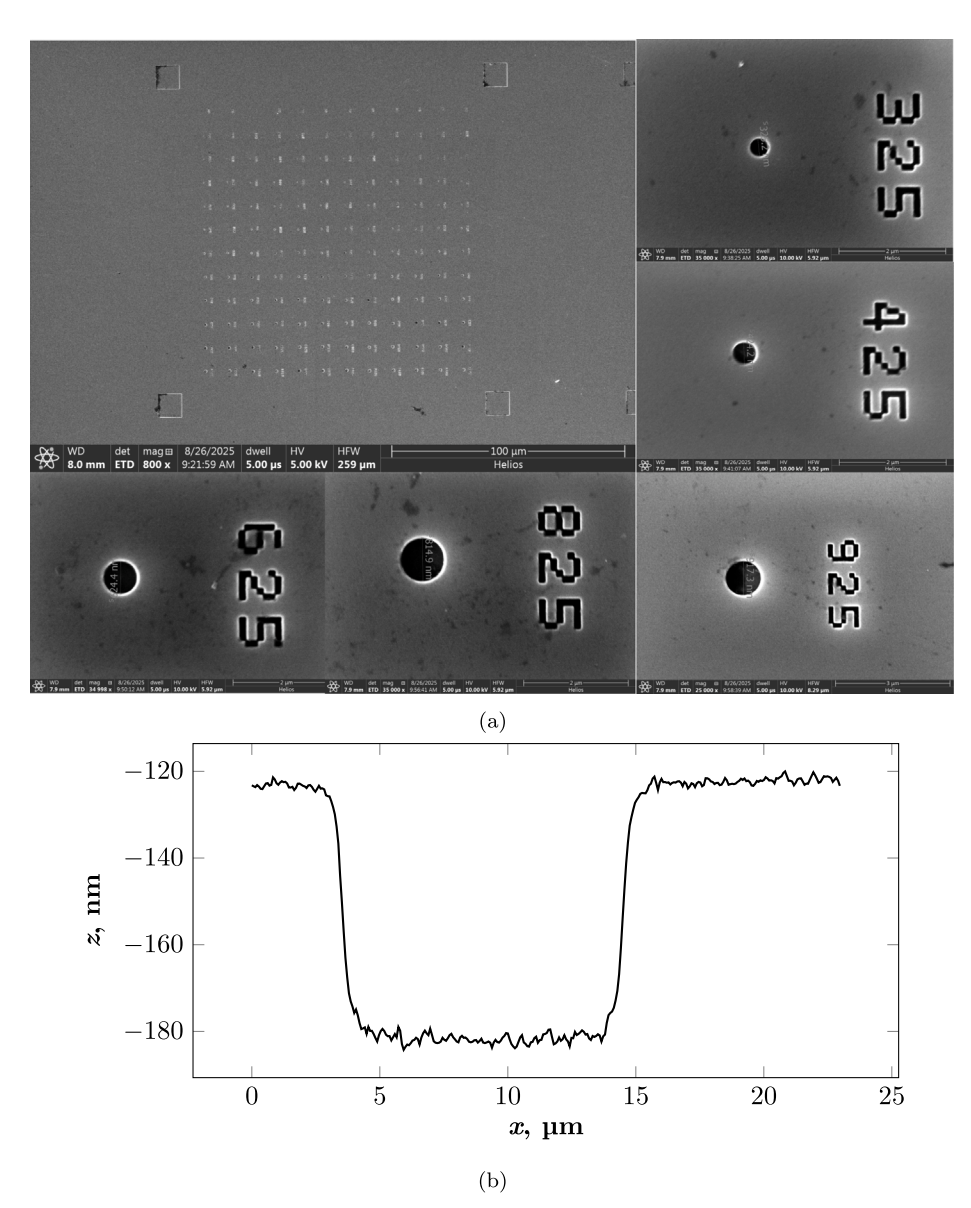
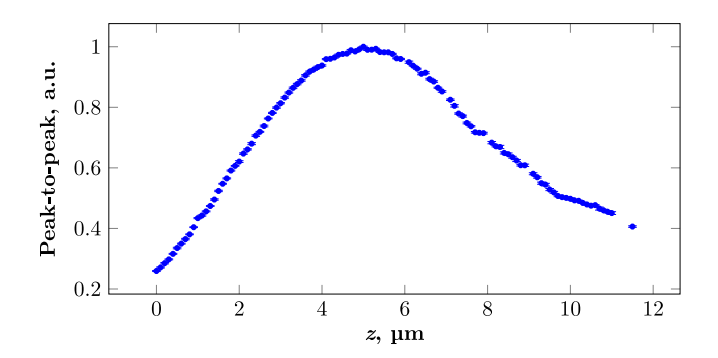


Fig. E.17. Sample measurements. (a) SEM images of the etched pits, (b) profile of an etched structure measured using a white light interferometer.



**Fig. F.18.** Reduction in peak-to-peak of the differential signal as a function of axial position of the sample. The plot is normalised using the maximum peak-to-peak value.

the measurements, we see that the peak-to-peak reduces to 90% of the maximum value when the sample is moved axially by 1.48  $\mu$ m.

### Data availability

Data will be made available on request.

### References

- IEEE International Roadmap for Devices and Systems, Metrology, Inst. Electr. Electron. Eng. (2023) http://dx.doi.org/10.60627/ff6x-d213.
- [2] N. Orji, M. Badaroglu, B. Barnes, et al., Metrology for the next generation of semiconductor devices, Nat. Electron. 1 (2018) 532–547, http://dx.doi.org/10. 1038/s41928-018-0150-9.
- [3] F. Priolo, T. Gregorkiewicz, T.F. Krauss, Silicon nanostructures for photonics and photovoltaics, Nature Nanotechnology 9 (1) (2014) 19–32, http://dx.doi.org/10. 1038/nnano.2013.271.
- [4] A.L.M. Reddy, S.R. Gowda, M.M. Shaijumon, P.M. Ajayan, Hybrid nanostructures for energy storage applications, Adv. Mater. 24 (37) (2012) 5045–5064, http: //dx.doi.org/10.1002/adma.201104502.
- [5] M. Shafique, X. Luo, Nanotechnology in transportation vehicles: An overview of its applications, environmental, health and safety concerns, Materials 12 (15) (2019) http://dx.doi.org/10.3390/ma12152493.
- [6] A. Bhat, S. Budholiya, S.A. Raj, M.T.H. Sultan, D. Hui, A.U.M. Shah, S.N.A. Safri, Review on nanocomposites based on aerospace applications, Nanotechnol. Rev. 10 (1) (2021) 237–253, http://dx.doi.org/10.1515/ntrev-2021-0018.

- [7] A.A. Yetisgin, S. Cetinel, M. Zuvin, A. Kosar, O. Kutlu, Therapeutic nanoparticles and their targeted delivery applications, Molecules 25 (9) (2020) http://dx.doi. org/10.3390/molecules25092193.
- [8] M.J. Mitchell, M.M. Billingsley, R.M. Haley, M.E. Wechsler, N.A. Peppas, R. Langer, Engineering precision nanoparticles for drug delivery, Nat. Rev. Drug Discov. 20 (2) (2021) 101–124, http://dx.doi.org/10.1038/s41573-020-0090-8.
- [9] W.A.D.M. Jayathilaka, K. Qi, Y. Qin, A. Chinnappan, W. Serrano-García, C. Baskar, H. Wang, J. He, S. Cui, S.W. Thomas, S. Ramakrishna, Significance of nanomaterials in wearables: A review on wearable actuators and sensors, Adv. Mater. 31 (7) (2019) 1805921, http://dx.doi.org/10.1002/adma.201805921.
- [10] W. Häßler-Grohne, D. Hüser, K.-P. Johnsen, C.G. Frase, H. Bosse, Current limitations of SEM and AFM metrology for the characterization of 3D nanostructures, Meas. Sci. Technol. 22 (9) (2011) 094003, http://dx.doi.org/10.1088/0957-0233/22/9/094003.
- [11] R.B. Bergmann, M. Kalms, C. Falldorf, Optical in-process measurement: Concepts for precise, fast and robust optical metrology for complex measurement situations, Appl. Sci. 11 (22) (2021) http://dx.doi.org/10.3390/app112210533.
- [12] Y. Shimizu, L.-C. Chen, D.W. Kim, X. Chen, X. Li, H. Matsukuma, An insight into optical metrology in manufacturing, Meas. Sci. Technol. 32 (4) (2021) 042003, http://dx.doi.org/10.1088/1361-6501/abc578.
- [13] A.C. Diebold, A. Antonelli, N. Keller, Perspective: Optical measurement of feature dimensions and shapes by scatterometry, APL Mater. 6 (5) (2018) 058201, http://dx.doi.org/10.1063/1.5018310.
- [14] N. Kumar, P. Petrik, G.K.P. Ramanandan, O.E. Gawhary, S. Roy, S.F. Pereira, W.M.J. Coene, H.P. Urbach, Reconstruction of sub-wavelength features and nanopositioning of gratings using coherent Fourier scatterometry, Opt. Express 22 (20) (2014) 24678–24688, http://dx.doi.org/10.1364/OE.22.024678.
- [15] S. Roy, A.C. Assafrao, S.F. Pereira, H.P. Urbach, Coherent Fourier scatterometry for detection of nanometer-sized particles on a planar substrate surface, Opt. Express 22 (11) (2014) 13250–13262. http://dx.doi.org/10.1364/OF.22.013250.
- [16] S. Soman, R. Horsten, T. Scholte, S.F. Pereira, Multi-beam coherent Fourier scatterometry, Meas. Sci. Technol. 35 (7) (2024) http://dx.doi.org/10.1088/ 1361-6501/ad3b2a.
- [17] C.J. Sheppard, Scanning confocal microscopy, Encycl. Opt. Eng. (2003) 2525–2544
- [18] C. Leone, S. Genna, V. Tagliaferri, Fibre laser cutting of CFRP thin sheets by multi-passes scan technique, Opt. Lasers Eng. 53 (2014) 43–50, http://dx.doi. org/10.1016/j.optlaseng.2013.07.027.
- [19] X.T. Nguyen, V.L. Dinh, H.-J. Lee, H. Kim, A high-definition LIDAR system based on two-mirror deflection scanners, IEEE Sensors J. 18 (2) (2018) 559–568, http://dx.doi.org/10.1109/JSEN.2017.2777500.
- [20] V.-F. Duma, K.-S. Lee, P. Meemon, J.P. Rolland, Experimental investigations of the scanning functions of galvanometer-based scanners with applications in OCT, Appl. Opt. 50 (29) (2011) 5735–5749, http://dx.doi.org/10.1364/AO.50.005735.
- [21] T. Ando, N. Kodera, E. Takai, D. Maruyama, K. Saito, A. Toda, A high-speed atomic force microscope for studying biological macromolecules, Proc. Natl. Acad. Sci. 98 (22) (2001) 12468–12472, http://dx.doi.org/10.1073/pnas. 211400898.
- [22] R. Lane, Y. Vos, A.H. Wolters, L. van Kessel, S.E. Chen, N. Liv, J. Klumperman, B.N. Giepmans, J.P. Hoogenboom, Optimization of negative stage bias potential for faster imaging in large-scale electron microscopy, J. Struct. Biol.: X 5 (2021) 100046, http://dx.doi.org/10.1016/j.yjsbx.2021.100046.
- [23] TNO, 2011, URL https://www.tno.nl/publish/pages/7808/tno-leaflet-rapid-nanoparticle-scanner.pdf.
- [24] I. Veilleux, J.A. Spencer, D.P. Biss, D. Cote, C.P. Lin, In vivo cell tracking with video rate multimodality laser scanning microscopy, IEEE J. Sel. Top. Quantum Electron. 14 (1) (2008) 10–18, http://dx.doi.org/10.1109/JSTQE.2007.912751.

- [25] A. Paul, R. Wever, S. Soman, S. Pereira, Utilizing focused field as a probe for shape determination of subwavelength structures via coherent Fourier scatterometry, Phys. Rev. Appl. 23 (2) (2025) http://dx.doi.org/10.1103/PhysRevApplied. 23 024016
- [26] D. Kolenov, D. Davidse, J. Le Cam, S. Pereira, Convolutional neural network applied for nanoparticle classification using coherent scatterometry data, Appl. Opt. 59 (27) (2020) 8426–8433, http://dx.doi.org/10.1364/AO.399894.
- [27] K. Carlsson, Scanning and detection techniques used in a confocal scanning laser microscope, J. Microsc. 157 (1) (1990) 21–27, http://dx.doi.org/10.1111/j.1365-2818 1990 tb02943 x
- [28] M. Kumar, Y. Kozorovitskiy, Tilt-invariant scanned oblique plane illumination microscopy for large-scale volumetric imaging, Opt. Lett. 44 (7) (2019) 1706–1709, http://dx.doi.org/10.1364/OL.44.001706.
- [29] J. Montagu, Handbook of Optical and Laser Scanning, CRC Press Boca Raton, FL, USA, 2016, pp. 418–473, http://dx.doi.org/10.1201/9781315218243.
- [30] P.E. Verboven, Distortion correction formulas for pre-objective dual galvanometer laser scanning, Appl. Opt. 27 (20) (1988) 4172–4173, http://dx.doi.org/10.1364/ AO.27.004172.
- [31] J.S. Ehrmann, Optics for vector scanning, in: L. Beiser, G.F. Marshall (Eds.), Beam Deflection and Scanning Technologies, Vol. 1454, SPIE, International Society for Optics and Photonics, 1991, pp. 245–256, http://dx.doi.org/10.1117/12.28036.
- [32] ISO 21457:2008(E), Ophthalmic Optics and Instruments Reporting Aberrations of the Human Eye, Standard, International Organization for Standardization, 2008
- [33] S. Soman, S.F. Pereira, Aberration characterisation in coherent Fourier scatterometry, in: Optical Measurement Systems for Industrial Inspection XIV, 13567, 2025, pp. 557–564, http://dx.doi.org/10.1117/12.3062562.
- [34] N. Fukutake, A general theory of far-field optical microscopy image formation and resolution limit using double-sided feynman diagrams, Sci. Rep. 10 (1) (2020) 17644, http://dx.doi.org/10.1038/s41598-020-73584-1.
- [35] C. Sheppard, C. Cogswell, Three-dimensional image formation in confocal microscopy, J. Microsc. 159 (2) (1990) 179–194, http://dx.doi.org/10.1111/j.1365-2818 1990 tb04774 x
- [36] G. Bouwhuis, J. Spruit, Optical storage read-out of nonlinear disks, Appl. Opt. 29 (26) (1990) 3766–3768, http://dx.doi.org/10.1364/AO.29.003766.
- [37] S. Mekid, D. Vaja, Propagation of uncertainty: Expressions of second and third order uncertainty with third and fourth moments, Measurement 41 (6) (2008) 600-609, http://dx.doi.org/10.1016/j.measurement.2007.07.004.
- [38] S.W. Smith, The Scientist and Engineer's Guide to Digital Signal Processing, California Technical Publishing, USA, 1997.
- [39] D. Kolenov, I.E. Zadeh, R.C. Horsten, S.F. Pereira, Direct detection of polystyrene equivalent nanoparticles with a diameter of 21 nm using coherent Fourier scatterometry, Opt. Express 29 (11) (2021) 16487–16505, http://dx.doi.org/10. 1364/OE.421145.
- [40] BIPM, IEC, IFCC, ILAC, ISO, IUPAC, IUPAP, OIML, Evaluation of measurement data - guide to the expression of uncertainty in measurement, Jt. Comm. Guid. Metrol. JCGM 100: (2008) http://dx.doi.org/10.59161/JCGM100-2008E, Section 4.2–4.3.
- [41] S. Roy, M. Bouwens, L. Wei, S.F. Pereira, H.P. Urbach, P. van der Walle, High speed low power optical detection of sub-wavelength scatterer, Rev. Sci. Instrum. 86 (12) (2015) 123111, http://dx.doi.org/10.1063/1.4938183.
- [42] J.W. Goodman, Introduction to Fourier Optics, Roberts and Company publishers, 2005.
- [43] G. Dai, L. Koenders, J. Fluegge, M. Hemmleb, Fast and accurate: high-speed metrological large-range AFM for surface and nanometrology, Meas. Sci. Technol. 29 (5) (2018) 054012, http://dx.doi.org/10.1088/1361-6501/aaaf8a.